# Electrocatalytic Properties of Oxygen-Deficient Perovskites $Ca_3Fe_{3-x}Mn_xO_8$ (x=1-2) for Hydrogen Evolution Reaction

Kinithi M. K. Wickramaratne<sup>a</sup>, Surendra B. Karki<sup>a</sup>, Farshid Ramezanipour<sup>a,\*</sup>

<sup>a</sup>Department of Chemistry, University of Louisville, Louisville, Kentucky 40292, USA \*Corresponding author. Email: <a href="mailto:farshid.ramezanipour@louisville.edu">farshid.ramezanipour@louisville.edu</a>, Phone: (502) 852-7061 ORCID: 0000-0003-4176-1386

#### **Abstract**

We have demonstrated a systematic trend in electrocatalytic activity for the hydrogen evolution reaction (HER), and its correlations with the transition metal type, structural order, and electrical conductivity. The materials studied in this work, Ca<sub>3</sub>FeMn<sub>2</sub>O<sub>8</sub> (CaFe<sub>1/3</sub>Mn<sub>2/3</sub>O<sub>3-1/3</sub>), Ca<sub>3</sub>Fe<sub>1.5</sub>Mn<sub>1.5</sub>O<sub>8</sub>, and Ca<sub>3</sub>Fe<sub>2</sub>MnO<sub>8</sub>, belong to the family of oxygen-deficient perovskites and show a gradual increase in the ordering of oxygen-vacancies. Ca<sub>3</sub>FeMn<sub>2</sub>O<sub>8</sub> (CaFe<sub>1/3</sub>Mn<sub>2/3</sub>O<sub>3-1/3</sub>) contains randomly distributed oxygen vacancies, which begin to order in Ca<sub>3</sub>Fe<sub>1.5</sub>Mn<sub>1.5</sub>O<sub>8</sub>, and are fully ordered in Ca<sub>3</sub>Fe<sub>2</sub>MnO<sub>8</sub>. The gradual increase in the structural order is associated with a systematic enhancement of the electrocatalytic activity for HER in acidic conditions, Ca<sub>3</sub>FeMn<sub>2</sub>O<sub>8</sub> < Ca<sub>3</sub>Fe<sub>1.5</sub>Mn<sub>1.5</sub>O<sub>8</sub> < Ca<sub>3</sub>Fe<sub>2</sub>MnO<sub>8</sub>. While the improvement of the HER activity is also associated with an increase in the Fe-content, we have shown that the type of structural order plays a more important role. We demonstrated this effect by control experiments on an analogous material where all Mn was substituted by Fe, leading to a different type of structural order, showing an inferior HER activity compared to the above three materials. Furthermore, electrical conductivity studies in a wide range of temperatures, 25 - 800 °C, indicate that the trend in the electrical conductivity is the same as that of the HER activity. These findings reveal several important structure-property relationships and highlight the importance of synergistic effects in enhancing electrocatalytic properties.

## 1. Introduction

There is a clear need for alternative fuels to meet the energy demands of the future. Hydrogen is an attractive candidate given its high energy density and low carbon emission compared to gasoline and coal. 1, 2 Hydrogen is also essential to ammonia production for fertilizers which drive modern agriculture. The generation of hydrogen by electrochemical water-splitting is a promising method of hydrogen production. However, due to the slow kinetics of the two half-reactions of water-splitting, oxygen-evolution reaction (OER) and hydrogen-evolution reaction (HER), the development of sustainable electrocatalysts that can lower the overpotentials of these reactions is essential. In particular, stable, cost-effective, and earth-abundant electrocatalytic materials are highly desirable. Perovskite oxides have been studied for electrocatalytic applications due to their low cost, compositional flexibility, high intrinsic activity, and favorable stability. 3-5 Perovskite oxides have the general formula ABO<sub>3</sub>, where A-site ions can be alkali, alkaline-earth, or lanthanide cations, and B-site ions can be transition metal cations.

Recent studies on oxygen-deficient perovskite oxides have shown that they can be promising electrocatalysts for OER.<sup>3-5</sup> Various structures derived from the perovskite oxide family, which contain oxygen-vacancies, have shown notable electrocatalytic properties.<sup>6-8</sup> In some cases, the electrocatalytic activities of oxygen-deficient phases have been better than those of stoichiometric perovskites without oxygen-vacancies.<sup>7, 9, 10</sup> The oxygen-vacancies can be present in the material structure in an ordered or disordered fashion, leading to significant diversity in structure and properties.<sup>8, 11</sup> Oxygen-deficient perovskites have also been studied as electrocatalysts for HER.<sup>12</sup> An example is the  $Ca_{2-x}Sr_xFeMnO_{6-\delta}$  series, where changes in concentration and ordering of oxygen-vacancies are associated with a variation in the HER activity.<sup>13</sup> Another example is the vacancy-ordered LaCa<sub>2</sub>Fe<sub>2</sub>GaO<sub>8</sub>, which has the so-called bilayered brownmillerite structure, and

shows higher electrocatalytic activity for HER than La<sub>3</sub>Fe<sub>2</sub>GaO<sub>9</sub>, which does not contain oxygen-vacancies. <sup>14</sup> In another work, a series of perovskite oxides with general formula Nd<sub>0.5</sub>Ba<sub>0.5</sub>MnO<sub>3- $\delta$ </sub> were synthesized with variable amounts of oxygen-vacancies. It was observed that the oxygen-deficiency of  $\delta$  = 0.25 was optimum for obtaining an ordered structure, consisting of alternating MnO<sub>5</sub> square pyramids and MnO<sub>6</sub> octahedra. This particular phase also had the best HER activity compared to those with higher or lower degrees of oxygen-deficiency, which lacked the ordering in their structures. <sup>15</sup>

In this work, we have explored the variations in the structure, oxygen-vacancies, and electrocatalytic activities for HER in a series of oxygen-deficient perovskites, CaFe<sub>1-x</sub>Mn<sub>x</sub>O<sub>3-1/3</sub> (Ca<sub>3</sub>Fe<sub>3-x</sub>Mn<sub>x</sub>O<sub>8</sub>). Previous reports on these materials have been limited to the synthesis and some structural characterizations. <sup>16, 17</sup> Here, we investigate the systematic changes in electrocatalytic properties, to demonstrate that the gradual variation in the structure between Ca<sub>3</sub>FeMn<sub>2</sub>O<sub>8</sub> (CaFe<sub>1/3</sub>Mn<sub>2/3</sub>O<sub>3-1/3</sub>), Ca<sub>3</sub>Fe<sub>1.5</sub>Mn<sub>1.5</sub>O<sub>8</sub>, and Ca<sub>3</sub>Fe<sub>2</sub>MnO<sub>8</sub> is accompanied by an increase in the electrocatalytic activity. Furthermore, we have synthesized the Fe-only analog without manganese, to confirm that electrocatalytic properties rely not only on the iron content but also on the structural order and the synergistic effects. In addition, we have shown that the same systematic trend is present in the electrical conductivities, namely the increase in the electrical conductivity as the Fe content and structural order increase.

## 2. Experimental

**Synthesis and Characterization.** Polycrystalline samples of Ca<sub>3</sub>Fe<sub>2</sub>MnO<sub>8</sub>, Ca<sub>3</sub>Fe<sub>1.5</sub>Mn<sub>1.5</sub>O<sub>8</sub>, Ca<sub>3</sub>FeMn<sub>2</sub>O<sub>8</sub> (CaFe<sub>1/3</sub>Mn<sub>2/3</sub>O<sub>3-1/3</sub>), and Ca<sub>3</sub>Fe<sub>3</sub>O<sub>8-δ</sub> were synthesized in the air by solid-state synthesis method. Stoichiometric proportions of precursors, CaCO<sub>3</sub>, Fe<sub>2</sub>O<sub>3</sub>, and Mn<sub>2</sub>O<sub>3</sub> were

ground and mixed by agate mortar and pestle, and pressed into pellets. The pellets were heated at 1100 °C for two periods of 48 hours under an argon atmosphere, with intermediate grinding and palletization between the two heating periods. The heating and cooling rates of the furnace for all samples were set at 100 °C/h. The structures of the materials were studied using powder X-ray diffraction (XRD) collected at room temperature using Cu K $\alpha_1$  radiation ( $\lambda = 1.54056$  Å) on an Xray diffractometer equipped with a Johansson monochromator. The 2θ scan range was 20° - 80°, and measurements were done with a step size of 0.0167°. Rietveld refinements were carried out using the GSAS program <sup>18</sup> and EXPGUI interface. <sup>19</sup> For Ca<sub>3</sub>FeMn<sub>2</sub>O<sub>8</sub> (CaFe<sub>1/3</sub>Mn<sub>2/3</sub>O<sub>3-1/3</sub>), which has only three atomic positions, a total of 11 parameters were refined, while for Ca<sub>3</sub>Fe<sub>2</sub>MnO<sub>8</sub>, which has nine atomic positions, a total of 31 parameters were refined, including profile parameters, background, zero, x,y,z coordinates, U<sub>iso</sub>, and unit cell parameters. About Ca<sub>3</sub>Fe<sub>1.5</sub>Mn<sub>1.5</sub>O<sub>8</sub>, the wide diffraction peaks made it difficult to obtain reasonable U<sub>iso</sub> values. Numerous attempts at Rietveld refinements all led to unrealistic U<sub>iso</sub> values, given the very wide diffraction peaks. Nevertheless, all peak positions for Ca<sub>3</sub>Fe<sub>1.5</sub>Mn<sub>1.5</sub>O<sub>8</sub> are similar to those of the ordered material Ca<sub>3</sub>Fe<sub>2</sub>MnO<sub>8</sub>, and can be readily assigned to the orthorhombic structure, as shown in Figure S1.

The oxygen content was investigated using iodometric titrations. <sup>14</sup> A mixture of excess KI (2 g) and 50 mg of the sample was dissolved in 100 mL of argon-purged 1 M HCl and allowed to react overnight. Subsequently, 5 mL of the reacted mixture, containing the generated iodine, was extracted and titrated against 0.025 M Na<sub>2</sub>S<sub>2</sub>O<sub>3</sub> using a starch indicator (0.6 mL), which was added near the titration endpoint. The excess KI caused the reduction of metal cations into ions with the lowest stable oxidation state. By calculating the number of moles of titrant (Na<sub>2</sub>S<sub>2</sub>O<sub>3</sub>) required to titrate 5 mL of the titrand, we can determine the quantity of I<sub>2</sub> titrated by Na<sub>2</sub>S<sub>2</sub>O<sub>3</sub> (I<sub>2</sub> + 2S<sub>2</sub>O<sub>3</sub><sup>2-</sup>  $\rightarrow$ 

 $2I^{-} + S_4O_6^{2-}$ ). This value correlates directly with the quantity of oxygen lost during the reduction of metal ions. The total oxygen content was calculated by adding the oxygen that remained available (to maintain charge balance with reduced cations) to the oxygen that was lost during the reduction of metal ions. For each sample, the measurements were repeated three times to obtain the error. The oxygen content was found to be 8.003(5), 8.02(4), and 8.072(8) moles per formula unit for Ca<sub>3</sub>Fe<sub>2</sub>MnO<sub>8</sub>, Ca<sub>3</sub>Fe<sub>1.5</sub>Mn<sub>1.5</sub>O<sub>8</sub>, and Ca<sub>3</sub>FeMn<sub>2</sub>O<sub>8</sub> (CaFe<sub>1/3</sub>Mn<sub>2/3</sub>O<sub>3-1/3</sub>), respectively. The morphological analyses were performed on sintered pellets using a Field Emission Gun Scanning Electron Microscope FEI Nova600 FEG-SEM at various magnifications, 5000×, 2500×, and 1000×. The imaging process utilized an Everhart-Thornley Detector (EDT) with a consistent accelerating voltage of 10.00 kV. X-ray photoelectron spectroscopy (XPS) was performed using a ThermoFisher Scientific model NEXSA surface analysis system equipped with a micro-focused X-ray source (72 W, 12 kV) of monochromatic Al K $\alpha$  radiation (hv = 1486.6 eV). Transmission Electron Microscopy (TEM) was done using a 200 keV FEI Talos F200X Field Emission Gun microscope to investigate powders of the synthesized samples. Sample preparation involved the dispersion of the powder in a solvent, followed by sonication for uniform dispersion. A suspension droplet was subsequently placed onto a TEM grid, allowing controlled drying to establish a representative sample layer. Following grid insertion and optimization of imaging parameters, micrographs were captured at various magnifications.

The variable temperature (25 – 800 °C) electrical conductivity measurements were done using a two-probe DC technique on pellets that had been sintered at 1100 °C. Prior to measurements, gold paste was applied to the two sides of pellets and dried by heating for 3 hours at 800 °C. Gold wires attached to gold foils were used as electrodes and were positioned to make contact with gold-painted surfaces on each side. A voltage of 0.01 V was applied. Electrical conductivity

measurements were performed in the temperature range of 25-800 °C at ~100 °C intervals. The time required to achieve equilibrium conductivity at each measurement temperature was approximately 30 minutes. This was determined based on the observation of a plateau in the DC conductivity data at each temperature before moving to the next temperature. The heating and cooling rates for conductivity measurements were 3 °C/min. No uncommon hazards are noted.

Electrochemical measurements. The catalyst ink for electrochemical measurements was prepared using 35 mg of the catalyst material, 7 mg of carbon black powder, 40 µL of Nafion D-521 solution (5% w/w in water and 1-propanol), and 7 mL of Tetrahydrofuran (THF). The mixture was ultrasonically dispersed in water for 30 minutes. The drop-casting was done by placing two coats of 10 µl of the mixture onto the surface of a glassy carbon electrode (GCE) with a diameter of 5 mm and an area of 0.196 cm<sup>2</sup>, with a mass loading of 1.02 mg/cm<sup>2</sup>, followed by overnight airdrying. This catalyst-loaded electrode was used as the working electrode. Electrochemical measurements were done using a standard three-electrode electrochemical cell connected to a rotating disk electrode at 1600 rpm. HER experiments were done in 0.5 M H<sub>2</sub>SO<sub>4</sub>. A commercial Ag/AgCl in 4 M KCl was used as the reference electrode and a carbon electrode as the counter electrode. All potentials were iR corrected and converted to potential vs reversible hydrogen electrode (RHE) using the Nernst equation  $E_{vs\ RHE} = E_{vs\ Ag/AgCl} + 0.059pH + E_{vs\ Ag/AgCl}^0$ , where  $E^0_{vs} Ag/AgCl = 0.197 \text{ V}$  for saturated KCl. <sup>20, 21</sup> For each material, the electrocatalytic measurements were repeated at least three times, using at least two different batches synthesized independently. We found that errors for HER overpotentials from these measurements were in the range of 0.01 -0.02 V (i.e., 2-3%). We note that overpotential values were in the range of 0.51 V -0.64 V.

Chronopotentiometry was employed to study the stability of the catalyst under HER conditions (0.5 M H<sub>2</sub>SO<sub>4</sub>) using the same three-electrode setup and a constant current of 10 mA/cm<sup>2</sup>.

#### 3. RESULTS AND DISCUSSION

## 3.1. Crystal Structure

Crystal structures of these compounds were confirmed by Rietveld refinements using powder Xray diffraction, as shown in Figure 1. All three compounds Ca<sub>3</sub>FeMn<sub>2</sub>O<sub>8</sub>, Ca<sub>3</sub>Fe<sub>1.5</sub>Mn<sub>1.5</sub>O<sub>8</sub>, and Ca<sub>3</sub>Fe<sub>2</sub>MnO<sub>8</sub> belong to the oxygen-deficient perovskite family. The general formula of oxygendeficient perovskites is ABO<sub>3- $\delta$ </sub>. For any  $\delta$  value, the formula can be rewritten to show integer numbers (e.g., ABO<sub>2.5</sub> can be presented as A<sub>2</sub>B<sub>2</sub>O<sub>5</sub>, while ABO<sub>2.67</sub> can be rewritten as A<sub>3</sub>B<sub>3</sub>O<sub>8</sub>). However, the presentation of the formula does not necessarily indicate how the oxygen-vacancies are distributed. In this work, all three ABO<sub>3- $\delta$ </sub> materials have  $\delta = 1/3$ , leading to the formula ABO<sub>2.67</sub> (ABO<sub>3-1/3</sub>) or A<sub>3</sub>B<sub>3</sub>O<sub>8</sub>. But the arrangement of oxygen-vacancies is different in the three materials. The first material in the series Ca<sub>3</sub>FeMn<sub>2</sub>O<sub>8</sub> (CaFe<sub>1/3</sub>Mn<sub>2/3</sub>O<sub>3-1/3</sub>) is an oxygen-deficient perovskite where the oxygen-vacancies are distributed randomly (Figure 2a). Therefore, this compound has an average structure similar to that of a typical perovskite oxide. Regular perovskite oxides contain AO<sub>12</sub> and BO<sub>6</sub> polyhedral units. In Ca<sub>3</sub>FeMn<sub>2</sub>O<sub>8</sub> (CaFe<sub>1/3</sub>Mn<sub>2/3</sub>O<sub>3-1/3</sub>), most B-site metals have octahedral coordination (FeO<sub>6</sub>/MnO<sub>6</sub>), and the A-site metal Ca occupies the spaces between those octahedra and is mostly 12-coordinated (CaO<sub>12</sub>). However, there are also oxygen-vacancies that are randomly distributed in the material, lowering the coordination number of some of the metals in an arbitrary distribution. Ca<sub>3</sub>FeMn<sub>2</sub>O<sub>8</sub> (CaFe<sub>1/3</sub>Mn<sub>2/3</sub>O<sub>3-1/3</sub>) crystallizes in the cubic space group  $Pm\overline{3}m$ . The refined structural parameters are listed in Table 1.

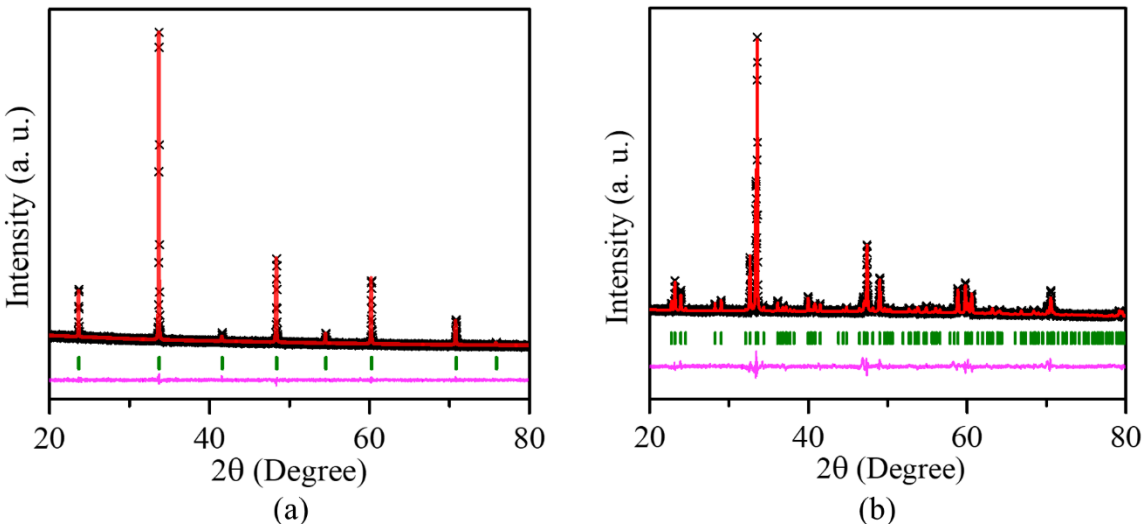


**Figure 1.** Rietveld refinement profiles using powder X-ray diffraction data of (a)  $Ca_3FeMn_2O_8$  ( $CaFe_{1/3}Mn_{2/3}O_{3-1/3}$ ) (disordered, Pm-3m) and (b)  $Ca_3Fe_2MnO_8$  (ordered,  $Pcm2_1$ ). The cross symbols, solid red line, olive vertical tick marks, and lower magenta line correspond to experimental data, the calculated pattern for the structural model, Bragg peak positions, and the difference plot, respectively.

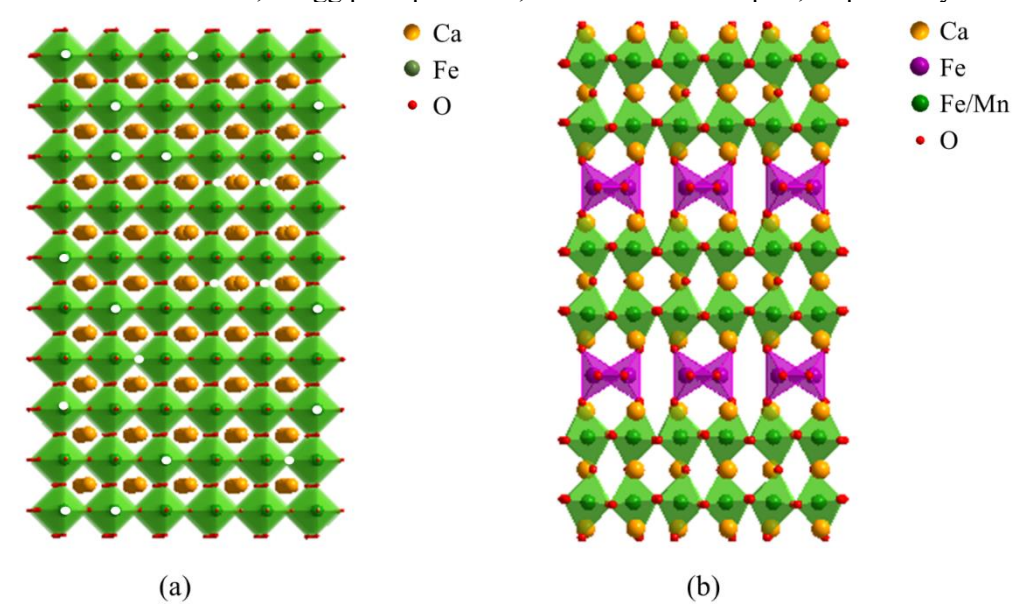


**Figure 2.** (a) Crystal structure of Ca<sub>3</sub>FeMn<sub>2</sub>O<sub>8</sub> (CaFe<sub>1/3</sub>Mn<sub>2/3</sub>O<sub>3-1/3</sub>), containing a random distribution of oxygen-vacancies, schematically represented by white circles. (b) Crystal structure of Ca<sub>3</sub>Fe<sub>1.5</sub>Mn<sub>1.5</sub>O<sub>8</sub> and Ca<sub>3</sub>Fe<sub>2</sub>MnO<sub>8</sub>, where oxygen-vacancies appear in every third layer and convert the octahedral coordination into tetrahedral.

As the Fe content increases, a structural order is observed. The peaks in the powder X-ray diffraction data (Figure S1) for Ca<sub>3</sub>Fe<sub>1.5</sub>Mn<sub>1.5</sub>O<sub>8</sub> (CaFe<sub>0.5</sub>Mn<sub>0.5</sub>O<sub>2.67</sub>) are consistent with a vacancy-ordered structure, the so-called Greiner phase<sup>22</sup> or bilayered brownmillerite (Figure 2b),<sup>16, 17, 23</sup>

although the peaks are broad. Given its broad diffraction peaks and the similarity of its crystallinity and particle size to those of the other two materials, this composition may represent a transition point between disordered and ordered structures. Further increase in the Fe-content results in Ca<sub>3</sub>Fe<sub>2</sub>MnO<sub>8</sub> (CaFe<sub>2/3</sub>Mn<sub>1/3</sub>O<sub>2.67</sub>), which has a vacancy-ordered bilayered brownmillerite structure (Figure 2b). We note that bilayered brownmillerite structure can be considered a subcategory of the oxygen-deficient perovskite family. This type of oxygen-deficient perovskite can be represented by the general formula AA'<sub>2</sub>B<sub>2</sub>B'O<sub>8</sub>, indicating different metal sites with different coordination geometries.<sup>24, 25</sup> Due to the presence of oxygen-vacancies in every third layer, the structure contains two crystallographically distinct B sites (referred to as B and B') with two different coordination geometries, namely octahedral BO<sub>6</sub> and tetrahedral B'O<sub>4</sub>. Also, as a result of the ordering of oxygen-vacancies, there are two types of A-sites (referred to as A and A'), which are 12-coordinated (located between BO<sub>6</sub> units) and 8-coordinated (residing between BO<sub>6</sub> and B'O<sub>4</sub> units). In Ca<sub>3</sub>Fe<sub>1.5</sub>Mn<sub>1.5</sub>O<sub>8</sub> and Ca<sub>3</sub>Fe<sub>2</sub>MnO<sub>8</sub>, both A and A' sites are occupied by Ca. About the B and B' sites, a previous study on a similar material (Ca<sub>3</sub>Fe<sub>1.8</sub>Mn<sub>1.2</sub>O<sub>8</sub>) suggested that the tetrahedral B'-site is occupied by Fe, while the octahedral B-site is occupied by a mixture of Fe and Mn.<sup>26</sup> We used a similar distribution of Fe and Mn in our refinements (Table 2). We also obtained X-ray photoelectron spectroscopy (XPS) data for all three materials. (Figure 3)

For iron, different oxidation states can be distinguished by XPS based on their binding energies and signature satellite peaks. For manganese, given the close overlap of binding energies of Mn<sup>3+</sup> and Mn<sup>4+</sup> peaks, we also did additional measurements of standard Mn<sub>2</sub>O<sub>3</sub> and MnO<sub>2</sub> samples. Based on these measurements, it is evident that manganese is present in a tetravalent state in all three materials, where the binding energies of 2p<sub>3/2</sub> and 2p<sub>1/2</sub> peaks are very similar to those of MnO<sub>2</sub>. They are also consistent with previously reported binding energies for tetravalent

manganese.<sup>27-30</sup> On the other hand, the binding energies in iron spectra are consistent with trivalent iron.<sup>31-33</sup> Also, the spectra show the signature satellite peak of Fe<sup>3+</sup> at 8-10 eV higher than the  $2p_{3/2}$  peak.<sup>34-36</sup>

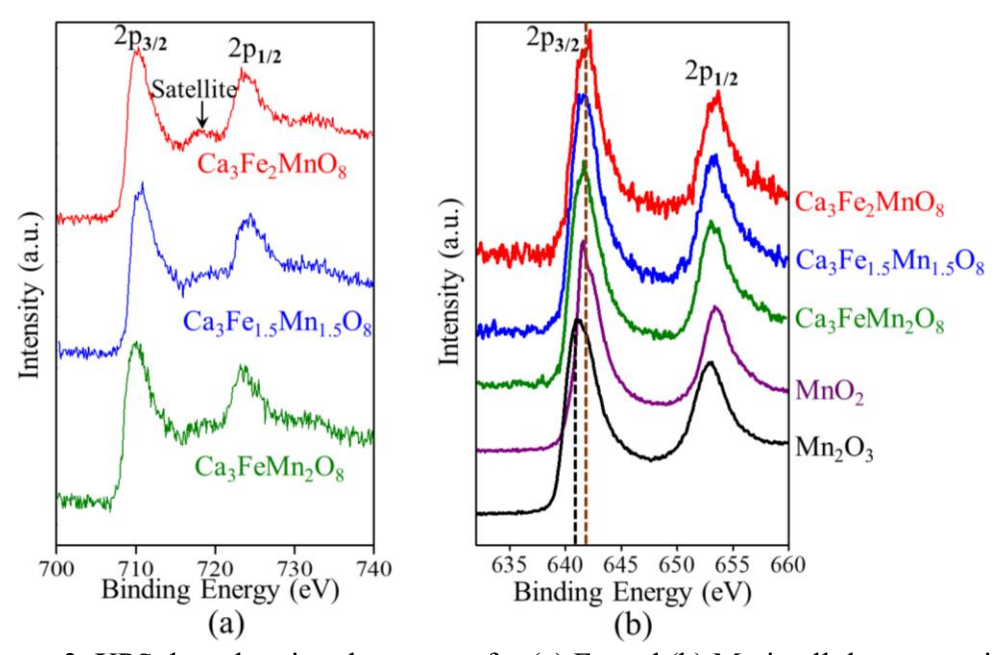


Figure 3. XPS data showing the spectra for (a) Fe and (b) Mn in all three materials.

While conventional X-ray diffraction cannot distinguish Mn and Fe, there are other methods that can provide information regarding the Mn/Fe occupancies. The XPS data, described above, indicate the presence of Mn<sup>4+</sup> and Fe<sup>3+</sup>. Crystal field stabilization energies indicate that Fe<sup>3+</sup> (d<sup>5</sup>) does not have a strong preference for either tetrahedral or octahedra sites. However, Mn<sup>4+</sup> (d<sup>3</sup>) has greater stability in octahedral site compared to tetrahedral, indicating that Mn<sup>4+</sup> prefers to reside in octahedral positions. In addition, Bond valence sum (BVS) calculations<sup>37</sup> confirm that Mn<sup>4+</sup> resides on an octahedral site. The calculated BVS values are 3.961 for the octahedral site and 3.076 for the tetrahedral site, indicating that the tetravalent Mn<sup>4+</sup> is preferentially located on the

octahedral site, while trivalent Fe<sup>3+</sup> is located on the tetrahedral site. These observations are also consistent with previous neutron studies of oxides containing both Fe and Mn, that show the octahedral site preference of manganese over iron.<sup>38, 39</sup>

**Table 1.** Refined structural parameters for  $Ca_3FeMn_2O_8$  ( $CaFe_{1/3}Mn_{2/3}O_{3-1/3}$ ) at room temperature using powder x-ray diffraction data. Space group: Pm-3m, a = 3.76009(4) Å,  $R_p = 0.0331$ ,  $wR_p = 0.0422$ 

Atom	X	У	Z	Occupancy	Multiplicity	$U_{iso}(A^2)$
Cal	0.5	0.5	0.5	1	1	0.038(1)
Fe1/Mn1	0	0	0	0.33/0.67	1	0.021(1)
O1	0.5	0	0	0.89	3	0.076(1)

**Table 2.** Refined structural parameters for  $Ca_3Fe_2MnO_8$  at room temperature by using powder X-ray diffraction data. Space group:  $Pcm2_1$ , a = 5.4839(1) Å, b = 11.1520(2) Å, c = 5.3643(1) Å,  $R_p = 0.0156$ ,  $wR_p = 0.0475$ 

Atom	X	у	z	Occupancy	Multiplicity	$U_{iso}(A^2)$
Cal	0.239(2)	0.5	0.523(2)	1	2	0.030(7)
Ca2	0.229(2)	0.1887(7)	0.524(2)	1	4	0.081(8)
Fe1	0.313(1)	0	0.054(2)	1	2	0.036(6)
Fe2/Mn1	0.255(1)	0.3287(7)	0	0.5/0.5	4	0.048(6)
O1	0.361(4)	0	0.498(9)	1	2	0.029(7)
O2	0.300(6)	0.5	0.034(7)	1	2	0.027(7)
О3	0.189(4)	0.138(1)	-0.048(4)	1	4	0.055(7)
O4	-0.024(5)	0.342(1)	0.178(4)	1	4	0.035(7)
O5	0.491(6)	0.312(1)	0.180(4)	1	4	0.052(7)

We also examined structural transitions at higher Fe content. By increasing the Fe content, we synthesized a material where all Mn was replaced by Fe. However, synthesis efforts under the same conditions as the other materials led to a different structure, i.e., regular brownmillerite, comprising a single octahedral layer, alternating with a tetrahedral layer. The product had the

formula  $Ca_3Fe_3O_{8-\delta}$ , where  $\delta = 0.5$ , (i.e.,  $Ca_2Fe_2O_5$ ) and crystallized in the *Pnma* space group, as previously reported.<sup>40, 41</sup> (Figure S2 and Table S1).

Oxygen contents of these materials were determined by iodometric titrations, indicating eight oxygens per formula unit for Ca<sub>3</sub>FeMn<sub>2</sub>O<sub>8</sub> (CaFe<sub>1/3</sub>Mn<sub>2/3</sub>O<sub>3-1/3</sub>), Ca<sub>3</sub>Fe<sub>1.5</sub>Mn<sub>1.5</sub>O<sub>8</sub>, and Ca<sub>3</sub>Fe<sub>2</sub>MnO<sub>8</sub>, (or 2.67 per formula unit if the formula is written as CaFe<sub>1-x</sub>Mn<sub>x</sub>O<sub>2.67</sub>) as matching the expected stoichiometries. The microstructures of these materials were also examined. Figure 4 shows the SEM images of sintered pellets of Ca<sub>3</sub>FeMn<sub>2</sub>O<sub>8</sub> (CaFe<sub>1/3</sub>Mn<sub>2/3</sub>O<sub>3-1/3</sub>), Ca<sub>3</sub>Fe<sub>1.5</sub>Mn<sub>1.5</sub>O<sub>8</sub>, and Ca<sub>3</sub>Fe<sub>2</sub>MnO<sub>8</sub>. The micrographs indicate that Ca<sub>3</sub>Fe<sub>2</sub>MnO<sub>8</sub> has the smallest crystallite size, as shown in Figure 4c. However, in general, the difference in crystallite size between the three materials is not considerable. This indicates that the broad peaks in X-ray diffraction data of Ca<sub>3</sub>Fe<sub>1.5</sub>Mn<sub>1.5</sub>O<sub>8</sub> cannot be due to small particle size. Also, transmission electron microscopy (TEM) data (Figure S3) indicate that the crystallinities of the three materials are not significantly different from each other.

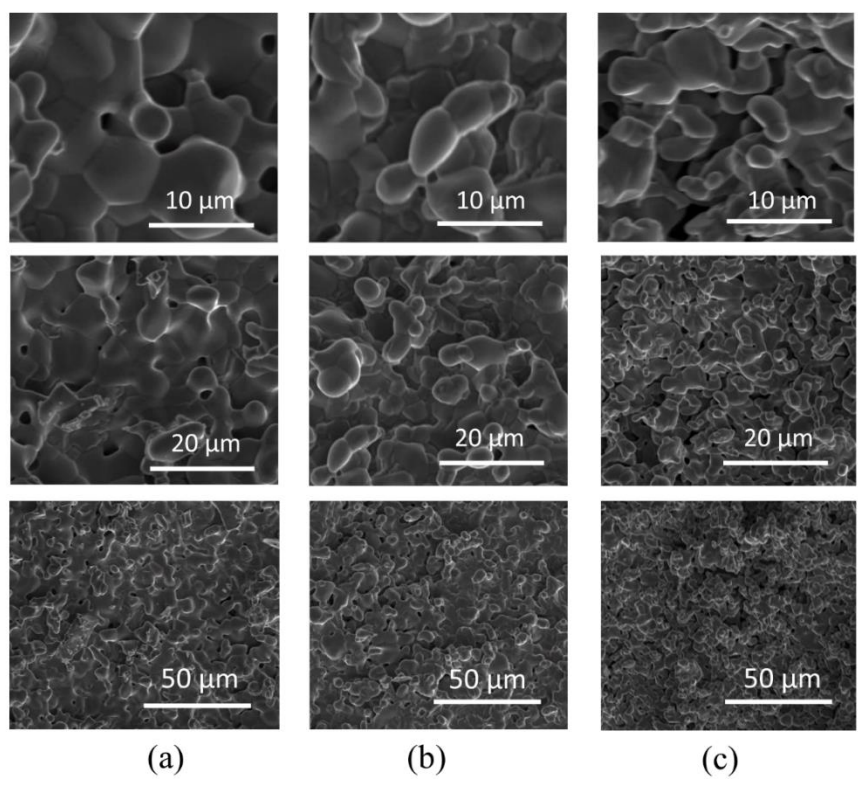


**Figure 4.** Scanning electron microscopy (SEM) images of (a)  $Ca_3FeMn_2O_8$  ( $CaFe_{1/3}Mn_{2/3}O_{3-1/3}$ ) (b)  $Ca_3Fe_{1.5}Mn_{1.5}O_8$  and (c)  $Ca_3Fe_2MnO_8$ .

# 3.2. Electrical conductivity

The electrical properties of these compounds were studied using the two-probe method<sup>42</sup> at variable temperatures from 25 °C to 800 °C. The direct current (DC) measurements involved finding the resistance (R) using the output current (I) upon applying a voltage (V) to calculate the conductivity ( $\sigma$ ) through Ohm's law.<sup>43, 44</sup> The following equation was used to calculate  $\sigma$ :

$$\sigma = \frac{l}{RA} = \frac{l}{V} \cdot \frac{l}{A} \tag{1}$$

Here, *l* indicates the thickness of the measured pellet, and *A* is the cross-sectional area of the pellet through which the current is applied.<sup>21</sup> Oxygen-deficient perovskites often show both electronic and ionic conductivities.<sup>45-47</sup> In some circumstances the electronic conductivity is more dominant when B-site cations have more than one oxidation state,<sup>48</sup> which is usually the case for transition metals. In the three materials studied in this work, the presence of manganese and iron with

variable oxidation states is responsible for the electronic conductivity. Electron transport is through the B-O-B pathway, where B is a transition metal with variable oxidation states.  $^{49, 50}$  Conduction happens due to an overlap between the 3d orbitals of transition metals and 2p orbitals of oxygens.  $^{49}$  The B-site cations can be modified to boost the electrical conductivity.  $^{4, 51}$  At room temperature,  $Ca_3Fe_2MnO_8$  shows the highest electrical conductivity compared to the other two materials. As shown in Figure 5a, the variable-temperature measurements for  $Ca_3FeMn_2O_8$  ( $CaFe_{1/3}Mn_{2/3}O_{3-1/3}$ ),  $Ca_3Fe_{1.5}Mn_{1.5}O_8$ , and  $Ca_3Fe_2MnO_8$  indicate a semiconducting behavior,  $^{52, 53}$  where conductivity increases gradually as a function of temperature. The results show the order of the electrical conductivity for the three compounds to be  $Ca_3FeMn_2O_8$  ( $CaFe_{1/3}Mn_{2/3}O_{3-1/3}$ )  $< Ca_3Fe_{1.5}Mn_{1.5}O_8$   $< Ca_3Fe_2MnO_8$ .

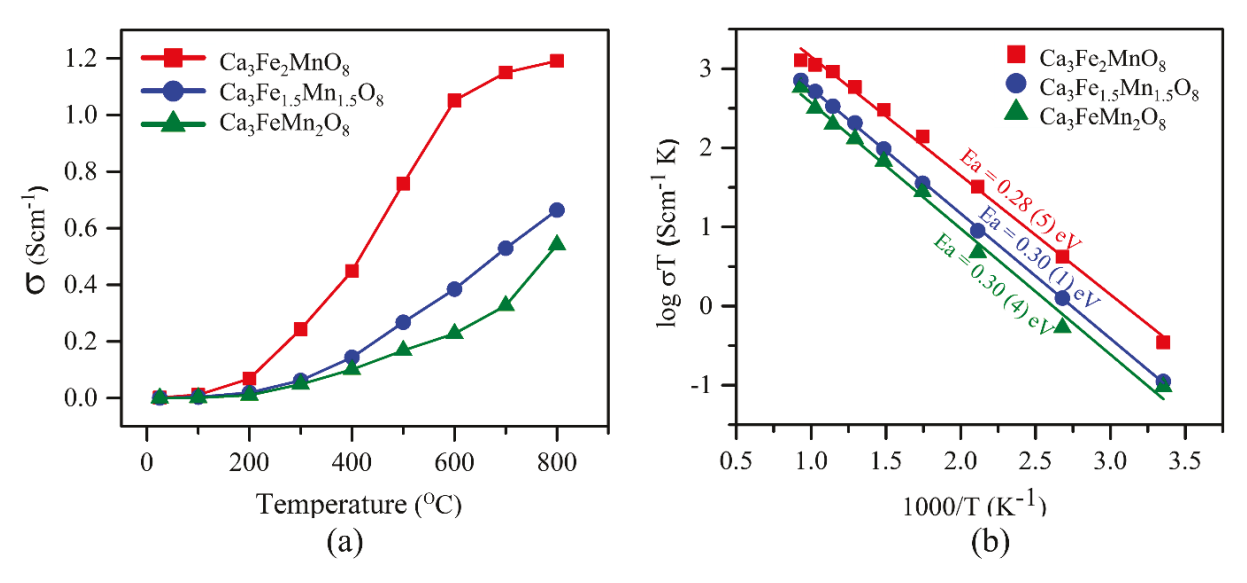


**Figure 5.** (a) Electrical conductivity as a function of temperature for  $Ca_3FeMn_2O_8$  ( $CaFe_{1/3}Mn_{2/3}O_{3-1/3}$ ),  $Ca_3Fe_{1.5}Mn_{1.5}O_8$ , and  $Ca_3Fe_2MnO_8$  (b) Arrhenius plots to determine the activation energies ( $E_a$ ) for the temperature-activated increase in conductivity.

As observed in Figure 5a and Table 3, the conductivity of Ca<sub>3</sub>Fe<sub>2</sub>MnO<sub>8</sub> is several folds higher than those of Ca<sub>3</sub>Fe<sub>1.5</sub>Mn<sub>1.5</sub>O<sub>8</sub> and Ca<sub>3</sub>FeMn<sub>2</sub>O<sub>8</sub>. This significant variation is due to structural differences and the Fe content in these materials. In Ca<sub>3</sub>Fe<sub>2</sub>MnO<sub>8</sub> and Ca<sub>3</sub>Fe<sub>1.5</sub>Mn<sub>1.5</sub>O<sub>8</sub>, the

oxygen-vacancies are arranged in an ordered manner, while Ca<sub>3</sub>FeMn<sub>2</sub>O<sub>8</sub> (CaFe<sub>1/3</sub>Mn<sub>2/3</sub>O<sub>3-1/3</sub>) is a disordered oxide where oxygen-vacancies have a random distribution. Also, Ca<sub>3</sub>Fe<sub>2</sub>MnO<sub>8</sub> has a higher Fe content than the other two materials. The electrical conductivity increases as the Fe content and the ordering of oxygen-vacancies increase. Figure 5b was used for fitting with the Arrhenius equation to calculate the activation energy (E<sub>a</sub>) for thermally activated conductivity. The Arrhenius equation can be expressed as:<sup>44, 54, 55</sup>

$$\sigma T = \sigma^0 e^{-\frac{E_a}{KT}}$$
 (2)

where  $\sigma^{\circ}$  is a pre-exponential factor and a characteristic of a material, and  $E_a$ , k, and T are the activation energy, Boltzmann constant, and absolute temperature, respectively. The activation energy ( $E_a$ ) for the change in conductivity as a function of temperature can be calculated from the slope of the line of best fit in the log  $\sigma T$  versus 1000/T plot. As shown in Figure 5b, the activation energies for the three materials are similar.

**Table 3.** Room temperature electrical conductivity and activation energies.

	Electrical conductivity at	Activation energy (eV)				
	room temperature (S/cm)					
Ca <sub>3</sub> FeMn <sub>2</sub> O <sub>8</sub>	$3.2 \times 10^{-4}$	0.30(4)				
$Ca_{3}Fe_{1.5}Mn_{1.5}O_{8}$	$3.73 \times 10^{-4}$	0.30(1)				
$Ca_3Fe_2MnO_8$	$1.16 \times 10^{-3}$	0.28(5)				

## 3.3. Electrocatalytic Activity for Hydrogen Evolution Reaction

To drive the hydrogen evolution reaction (HER) at a considerable rate, an excess potential, i.e., overpotential, must be applied to overcome the sluggish reaction kinetics.<sup>1, 56, 57</sup> Therefore, designing efficient, cost-effective, and highly stable electrocatalysts is crucial to improving the reaction kinetics and lowering the overpotential. The HER mechanism in an acidic medium involves a first step, called the Volmer step, where protons (H<sup>+</sup>) are supplied from the hydronium

ion (H<sub>3</sub>O<sup>+</sup>) to combine with an electron and form adsorbed hydrogen (H<sub>ads</sub>) intermediate species.<sup>1, 58</sup> The next step can be either Heyrovsky or Tafel reaction. In the Heyrovsky step, the adsorbed hydrogen intermediate (H<sub>ads</sub>) is combined with an electron as well as a proton (H<sup>+</sup>) to produce a hydrogen molecule. In the Tafel step two neighboring absorbed hydrogen atoms (H<sub>ads</sub>) chemically bond with each other to generate a hydrogen molecule.<sup>12, 59</sup> Acidic conditions boost the HER, but there are often problems with the metal oxide stability in an acidic environment.<sup>4, 9, 60</sup>

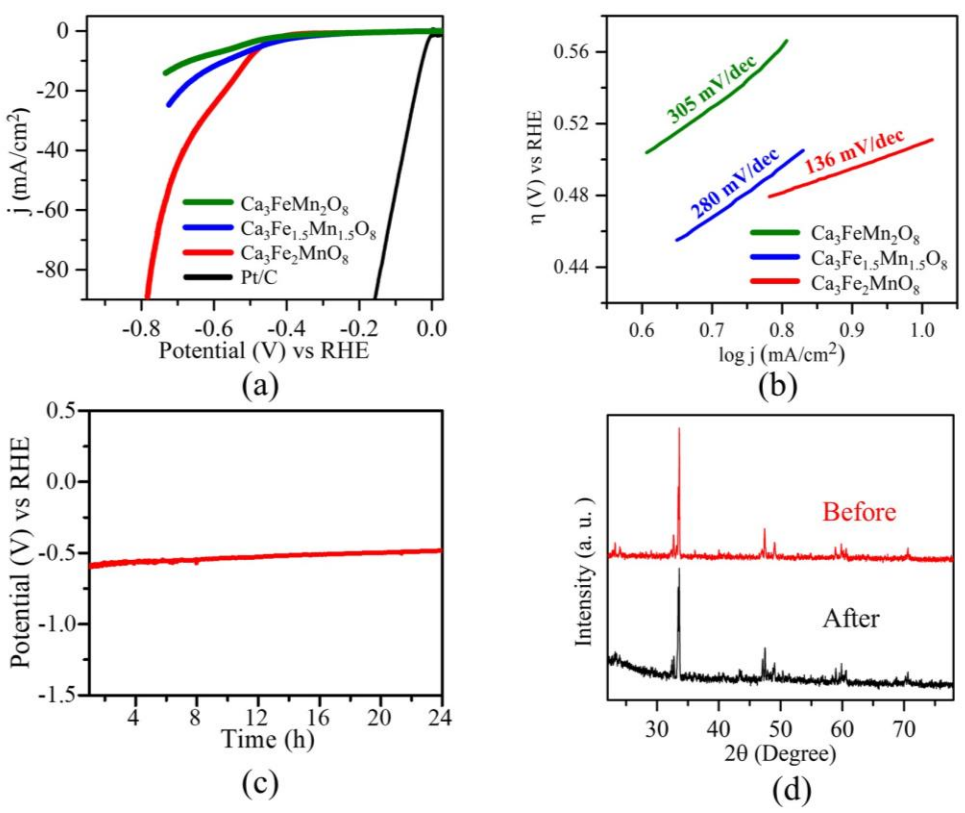


**Figure 6.** (a) Polarization curves for HER in 0.5 M H<sub>2</sub>SO<sub>4</sub>. (b) Tafel plots and slopes. (c) Chronopotentiometry data for the best performing material Ca<sub>3</sub>Fe<sub>2</sub>MnO<sub>8</sub> (d) X-ray diffraction data for Ca<sub>3</sub>Fe<sub>2</sub>MnO<sub>8</sub> before and after 100 cycles of HER.

In our work, the three materials show good electrocatalytic activity for acidic HER. Figure 6a shows the polarization curves for the HER activities of the three compounds in 0.5 M H<sub>2</sub>SO<sub>4</sub>. HER activities for Ca<sub>3</sub>FeMn<sub>2</sub>O<sub>8</sub> (CaFe<sub>1/3</sub>Mn<sub>2/3</sub>O<sub>3-1/3</sub>), Ca<sub>3</sub>Fe<sub>1.5</sub>Mn<sub>1.5</sub>O<sub>8</sub>, and Ca<sub>3</sub>Fe<sub>2</sub>MnO<sub>8</sub> vary

disordered material with the least iron-content,  $Ca_3FeMn_2O_8$  ( $CaFe_{1/3}Mn_{2/3}O_{3-1/3}$ ), shows the highest overpotential of 0.664 V at 10 mA/cm<sup>2</sup>. The overpotential is decreased as the Fe-content and the degree of vacancy-order increase, where  $Ca_3Fe_{1.5}Mn_{1.5}O_8$  and  $Ca_3Fe_2MnO_8$  show respective overpotentials of 0.570 V and 0.509 V at 10 mA/cm<sup>2</sup>. To determine whether this decrease in overpotential is only due to the Fe-content, or the structure-type also has an effect, we also examined  $Ca_3Fe_3O_{8-\delta}$  ( $\delta=0.5$ ), which has a different structure (Figure S2) and shows an overpotential of 0.683 V under the same conditions (Figure S4). This indicates that the Fe-content is not the only parameter that affects the HER activity, and the type of structural order is also an important factor.

A comparison to the literature, shows that there are some catalysts, particularly composites and nanomaterials, such as WO<sub>3</sub> nanoplates (estimated overpotential -0.117 V)<sup>61</sup> and MoO<sub>3-y</sub> nanofilms (approximate overpotential -0.201 V),<sup>62</sup> which show lower overpotentials than Ca<sub>3</sub>Fe<sub>2</sub>MnO<sub>8</sub>. However, the catalytic activity of Ca<sub>3</sub>Fe<sub>2</sub>MnO<sub>8</sub> ( $\eta_{10}$ = -0.509 V) in the acidic medium is better than those of several other catalysts reported previously. For example, the reported overpotentials for Sr<sub>2</sub>LaMn<sub>2</sub>O<sub>7</sub> ( $\eta_{10}$ = -0.589 V)<sup>63</sup>, Ca<sub>2</sub>LaMn<sub>2</sub>O<sub>7</sub> ( $\eta_{10}$ = -0.595 V)<sup>63</sup>, Sr<sub>2</sub>LaFeMnO<sub>7</sub> ( $\eta_{10}$ = -0.693 V)<sup>64</sup>, Sr<sub>2</sub>LaCoMnO<sub>7</sub> ( $\eta_{10}$ = -0.612 V)<sup>64</sup>, SrLaFeO<sub>4</sub> ( $\eta_{10}$ = -0.730 V),<sup>6</sup> SrLaCo<sub>0.5</sub>Fe<sub>0.5</sub>O<sub>4</sub> ( $\eta_{10}$ = -0.570 V),<sup>6</sup> SrLaCoO<sub>4-6</sub> ( $\eta_{10}$ = -0.547 V),<sup>6</sup> and WO<sub>3</sub> ( $\eta_{10}$ = -0.637 V)<sup>65</sup> are larger than that of Ca<sub>3</sub>Fe<sub>2</sub>MnO<sub>8</sub>. Chronopotentiometry experiments for the best-performing material, Ca<sub>3</sub>Fe<sub>2</sub>MnO<sub>8</sub>, are shown in Figure 6c, showing little change in the potential for 24 hours. To investigate the reaction kinetics, Tafel plots derived from polarization curves were used. The Tafel equation can be described as  $\eta$  = a + blog j, where  $\eta$  is the overpotential, and j is the current density.<sup>66,67</sup> A smaller slope of the Tafel plot signifies faster reaction kinetics for HER.<sup>1,68,69</sup> The Tafel slopes for Ca<sub>3</sub>FeMn<sub>2</sub>O<sub>8</sub>

(CaFe<sub>1/3</sub>Mn<sub>2/3</sub>O<sub>3-1/3</sub>), Ca<sub>3</sub>Fe<sub>1.5</sub>Mn<sub>1.5</sub>O<sub>8</sub>, and Ca<sub>3</sub>Fe<sub>2</sub>MnO<sub>8</sub> are 305 mV/dec, 280 mV/dec, and 136 mV/dec, respectively, as shown in Figure 6b. Ca<sub>3</sub>Fe<sub>2</sub>MnO<sub>8</sub> shows the smallest Tafel slope among the three materials, which is consistent with its high HER activity, and indicates faster reaction kinetics. These results show that there is a correlation between HER kinetics and the ordering of oxygen vacancies, as well as iron-content in the material. Also, X-ray diffraction data before and after the HER experiment (Figure 6d) show little change, indicating that Ca<sub>3</sub>Fe<sub>2</sub>MnO<sub>8</sub> retains its structural integrity upon the HER electrocatalytic process.

We have also studied the double-layer capacitance,  $C_{dl}$ , obtained from cyclic voltammetry (CV) measurements in the non-Faradaic region (Figure 7a-c). The importance of  $C_{dl}$  is that it is directly proportional to the electrochemically active surface area.<sup>4, 13, 70</sup> The  $C_{dl}$  values are found using a correlation with current density (j), through the formula  $C_{dl} = j_{avg}/v$ , where v is the scan rate, and  $j_{avg}$  is the average of the absolute values of  $j_{anodic}$  and  $j_{cathodic}$  at the middle potential of the CV obtained in the nonfaradic region.<sup>71</sup> The slope of  $j_{avg}$  vs v gives the  $C_{dl}$  value for each compound.<sup>21, 72</sup> As shown in Figure 7d, the  $C_{dl}$  values follow the same trend as the electrocatalytic activity, where the most active catalyst,  $C_{a3}F_{e2}MnO_8$ , also has the highest  $C_{dl}$  value.

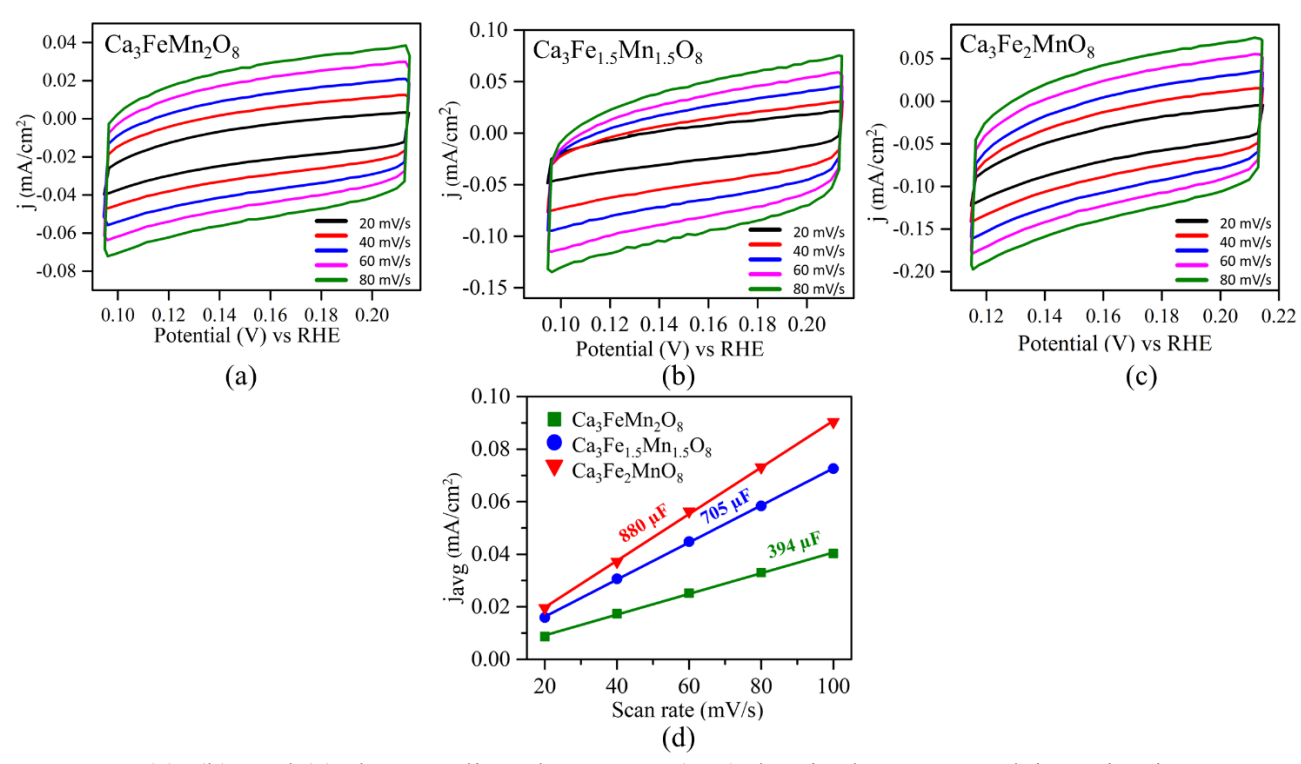


**Figure 7.** (a), (b), and (c) show cyclic voltammetry (CV) data in the non-Faradaic region in 0.5 M  $H_2SO_4$ . (d) The plot of  $j_{avg}$  obtained from the above CVs as a function of scan rate, where the slope is the double-layer capacitance,  $C_{dl}$ .

The results discussed above suggest that the following factors contribute to the electrocatalytic activity. Firstly, the higher HER activity of Ca<sub>3</sub>Fe<sub>2</sub>MnO<sub>8</sub> compared to other materials in this series may be related to the iron-content. This can be correlated with the electronegativity effect, since Fe has a higher electronegativity compared to Mn. Some researchers have noted that the increase in electronegativity will lower the energy of d orbitals in transition metals.<sup>73</sup> Lowering the d band energy will facilitate the overlap between the metal d and oxygen p orbitals, resulting in a higher electrocatalytic activity.<sup>74, 75</sup> However, the improved electrocatalytic properties of these materials are not only due to the iron content, but are also related to structural properties. This was confirmed by the investigation of the HER activity of Ca<sub>3</sub>Fe<sub>3</sub>O<sub>8-δ</sub>, which has a higher Fe-content but a different structure (Figure S2). This material showed an inferior electrocatalytic activity (Figure

S4) compared to Ca<sub>3</sub>Fe<sub>2</sub>MnO<sub>8</sub>, indicating the important effect of structure on the HER performance. The effect of structural order on enhancing the electrocatalytic activity has been observed in some other systems before.<sup>8, 9</sup> Finally, the electrical conductivity can also affect the electrocatalytic properties given the fact that HER involves the transfer of electrons. In the materials studied in this work, the trend in electrical conductivity is the same as the trend in electrocatalytic activity, indicating a correlation between these two properties.

#### 3.4. Conclusions

The effects of the transition metal type, structural order, and electrical conductivity on the improvement of electrocatalytic activity have been demonstrated in a series of oxygen-deficient perovskite oxides. A systematic trend in the HER performance is observed among the three materials,  $Ca_3FeMn_2O_8$  ( $CaFe_{1/3}Mn_{2/3}O_{3-1/3}$ )  $< Ca_3Fe_{1.5}Mn_{1.5}O_8 < Ca_3Fe_2MnO_8$ . The oxygenvacancy-disordered material Ca<sub>3</sub>FeMn<sub>2</sub>O<sub>8</sub> (CaFe<sub>1/3</sub>Mn<sub>2/3</sub>O<sub>3-1/3</sub>) shows the lowest HER activity, which can be gradually enhanced as the Fe-content and structural order increase in Ca<sub>3</sub>Fe<sub>1.5</sub>Mn<sub>1.5</sub>O<sub>8</sub> and Ca<sub>3</sub>Fe<sub>2</sub>MnO<sub>8</sub>. The latter two materials have a structure where the oxygenvacancies are ordered. The enhancement of the electrocatalytic performance is associated with higher iron-contents, which may be attributed to the larger electronegativity of Fe compared to Mn, that can enhance the adsorption of the reaction intermediates. However, the type of structural order is more important, as evident from the lower HER activity of an analogous material that only contains Fe, but has a different structure-type. In addition, electrical conductivity could play a role due to the need for electron transfer during the HER process. In the materials studied in this work, the trend for the increase in electrical conductivity is the same as that of the electrocatalytic activity.

## Acknowledgment

This work is supported by the National Science Foundation (NSF) under grant no. DMR-1943085.

#### **Conflict of Interests**

Authors declare no conflict of interests.

## **Associated Content**

Supporting Information Available: Powder X-ray diffraction data (PXRD) for  $Ca_3Fe_{1.5}Mn_{1.5}O_8$ ; PXRD, structure, refined structural parameters and HER polarization curve for  $Ca_3Fe_3O_{8-\delta}$  ( $\delta = 0.5$ , i.e.,  $Ca_2Fe_2O_5$ ); TEM images and electrochemical impedance spectroscopy data for  $Ca_3FeMn_2O_8$ ,  $Ca_3Fe_{1.5}Mn_{1.5}O_8$  and  $Ca_3Fe_2MnO_8$ . This information is available free of charge at the website: https://pubs.acs.org

#### References

- 1. Zhu, J.; Hu, L.; Zhao, P.; Lee, L. Y. S.; Wong, K.-Y., Recent advances in electrocatalytic hydrogen evolution using nanoparticles. *Chem. Rev.* **2019**, *120* (2), 851-918.
- 2. Turner, J.; Sverdrup, G.; Mann, M. K.; Maness, P. C.; Kroposki, B.; Ghirardi, M.; Evans, R. J.; Blake, D., Renewable hydrogen production. *Int. J. Energy Res.* **2008**, *32* (5), 379-407.
- 3. Suntivich, J.; May, K. J.; Gasteiger, H. A.; Goodenough, J. B.; Shao-Horn, Y., A perovskite oxide optimized for oxygen evolution catalysis from molecular orbital principles. *Science* **2011**, *334* (6061), 1383-1385.
- 4. Hona, R. K.; Ramezanipour, F., Remarkable Oxygen-Evolution Activity of a Perovskite Oxide from the  $Ca_{2-x}Sr_xFe_2O_{6-\delta}$  Series. *Angew Chem.* **2019**, *131* (7), 2082-2085.
- 5. Karki, S. B.; Hona, R. K.; Yu, M.; Ramezanipour, F., Enhancement of Electrocatalytic Activity as a Function of Structural Order in Perovskite Oxides. *ACS Catal.* **2022**, *12*, 10333-10337.
- 6. Alom, M. S.; Ramezanipour, F., Layered Oxides  $SrLaFe_{1-x}Co_xO_{4-\delta}$  (x=0-1) as Bifunctional Electrocatalysts for Water-Splitting. *ChemCatChem* **2021**, *13* (15), 3510-3516.
- 7. Kim, J.; Yin, X.; Tsao, K.-C.; Fang, S.; Yang, H., Ca<sub>2</sub>Mn<sub>2</sub>O<sub>5</sub> as oxygen-deficient perovskite electrocatalyst for oxygen evolution reaction. *J. Am. Chem. Soc.* **2014**, *136* (42), 14646-14649.
- 8. Karki, S. B.; Andriotis, A. N.; Menon, M.; Ramezanipour, F., Bifunctional Water-Splitting Electrocatalysis Achieved by Defect Order in LaA<sub>2</sub>Fe<sub>3</sub>O<sub>8</sub> (A= Ca, Sr). *ACS Appl. Energy Mater.* **2021**, *4* (11), 12063-12066.
- 9. Hona, R. K.; Ramezanipour, F., Effect of the oxygen vacancies and structural order on the oxygen evolution activity: a case study of SrMnO<sub>3- $\delta$ </sub> featuring four different structure types. *Inorg. Chem.* **2020**, 59 (7), 4685-4692.
- 10. Sun, Q.; Dai, Z.; Zhang, Z.; Chen, Z.; Lin, H.; Gao, Y.; Chen, D., Double perovskite PrBaCo<sub>2</sub>O<sub>5.5</sub>: An efficient and stable electrocatalyst for hydrogen evolution reaction. *J. Power Sources* **2019**, *427*, 194-200.

- 11. Hona, R. K.; Karki, S. B.; Cao, T.; Mishra, R.; Sterbinsky, G. E.; Ramezanipour, F., Sustainable oxide electrocatalyst for hydrogen-and oxygen-evolution reactions. *ACS Catal.* **2021**, *11* (23), 14605-14614.
- 12. Alom, M. S.; Kananke-Gamage, C. C.; Ramezanipour, F., Perovskite Oxides as Electrocatalysts for Hydrogen Evolution Reaction. *ACS omega* **2022**, *7* (9), 7444-7451.
- 13. Hona, R. K.; Karki, S. B.; Ramezanipour, F., Oxide Electrocatalysts Based on Earth-Abundant Metals for Both Hydrogen-and Oxygen-Evolution Reactions. *ACS Sustain. Chem. Eng.* **2020**, *8* (31), 11549-11557.
- 14. Wickramaratne, K. M.; Ramezanipour, F., Impact of oxygen-vacancies on electrical conductivity and electrocatalytic activity of La<sub>3-x</sub>Ca<sub>x</sub>Fe<sub>2</sub>GaO<sub>9- $\delta$ </sub> (x= 0, 2;  $\delta$ = 0, 1). *Solid State Sci.* **2023**, *141*, 107208.
- 15. Wang, J.; Gao, Y.; Chen, D.; Liu, J.; Zhang, Z.; Shao, Z.; Ciucci, F., Water splitting with an enhanced bifunctional double perovskite. *ACS Catal.* **2018**, *8* (1), 364-371.
- 16. Rao, C.; Gopalakrishnan, J.; Vidyasagar, K.; Ganguli, A.; Ramanan, A.; Ganapathi, L., Novel metal oxides prepared by ingenious synthetic routes. *J. Mater. Res.* **1986**, *I* (2), 280-294.
- 17. Vidyasagar, K.; Ganapathi, L.; Gopalakrishnan, J.; Rao, C. R., Novel oxygen vacancy-ordered phases of  $Ca_2Fe_{2-x}Mn_xO_5$  prepared by the topotactic reduction of the perovskite oxides,  $Ca_3Fe_{3-x}Mn_xO_{9-y}$  (0< y< 1.5). *J Chem Soc Chem Commun* **1986**, (6), 449-451.
- 18. Larson, A. C.; Von Dreele, R. B., General structure analysis system (GSAS)(Report LAUR 86-748). Los Alamos, New Mexico: Los Alamos National Laboratory 2004.
- 19. Toby, B. H., EXPGUI, a graphical user interface for GSAS. *J. Appl. Crystallogr.* **2001,** *34* (2), 210-213.
- 20. Jia, Y.; Zhang, L.; Du, A.; Gao, G.; Chen, J.; Yan, X.; Brown, C. L.; Yao, X., Defect graphene as a trifunctional catalyst for electrochemical reactions. *Adv Mater* **2016**, *28* (43), 9532-9538.
- 21. Karki, S. B.; Ramezanipour, F., Pseudocapacitive Energy Storage and Electrocatalytic Hydrogen-Evolution Activity of Defect-Ordered Perovskites  $Sr_xCa_{3-x}GaMn_2O_8$  (x= 0 and 1). *ACS Appl. Energy Mater.* **2020,** *3* (11), 10983-10992.
- 22. Grenier, J.-C.; Darriet, J.; Pouchard, M.; Hagenmuller, P., Mise en evidence d'une nouvelle famille de phases de type perovskite lacunaire ordonnee de formule A<sub>3</sub>M<sub>3</sub>O<sub>8</sub> (AMO<sub>2,67</sub>). *Mater. Res. Bull.* **1976**, *11* (10), 1219-1225.
- 23. Battle, P.; Gibb, T.; Lightfoot, P., The crystal and magnetic structures of Sr<sub>2</sub>LaFe<sub>3</sub>O<sub>8</sub>. *J. Solid State Chem.* **1990**, *84* (2), 237-244.
- 24. Luo, K.; Hayward, M. A., The synthesis and characterisation of LaCa<sub>2</sub>Fe<sub>2</sub>GaO<sub>8</sub>. *J. Solid State Chem.* **2013**, *198*, 203-209.
- 25. Hudspeth, J.; Goossens, D.; Studer, A. J.; Withers, R.; Norén, L., The crystal and magnetic structures of LaCa<sub>2</sub>Fe<sub>3</sub>O<sub>8</sub> and NdCa<sub>2</sub>Fe<sub>3</sub>O<sub>8</sub>. *J. Condens. Matter Phys.* **2009**, *21* (12), 124206.
- 26. Rodriguez-Carvajal, J.; Vallet-Regi, M.; Calbet, J. G., Perovskite threefold superlattices: a structure determination of the A<sub>3</sub>M<sub>3</sub>O<sub>8</sub> phase. *Mater. Res. Bull.* **1989**, *24* (4), 423-430.
- 27. Xia, W.; Pei, Z.; Leng, K.; Zhu, X., Research progress in rare earth-doped perovskite manganite oxide nanostructures. *Nanoscale Res. Lett.* **2020,** *15*, 1-55.
- 28. Li, S.; Wang, S.; Lu, Y.; Zhang, C.; Yang, X.; Gao, J.; Li, D.; Zhu, Y.; Liu, W., Exchange bias effect in hybrid improper ferroelectricity Ca2. 94Na<sub>0.06</sub>Mn<sub>2</sub>O<sub>7</sub>. *AIP Adv.* **2018**, 8 (1).
- 29. Bhowmick, S.; Mohanta, M. K.; Qureshi, M., Transcription methodology for rationally designed morphological complex metal oxides: a versatile strategy for improved electrocatalysis. *Sustain.* **2021**, *5* (24), 6392-6405.
- 30. Wang, M.; Chen, K.; Liu, J.; He, Q.; Li, G.; Li, F., Efficiently enhancing electrocatalytic activity of  $\alpha$ -MnO<sub>2</sub> nanorods/N-doped ketjenblack carbon for oxygen reduction reaction and oxygen evolution reaction using facile regulated hydrothermal treatment. *Catal.* **2018**,  $\delta$  (4), 138.
- 31. Yamashita, T.; Hayes, P., Analysis of XPS spectra of Fe<sup>2+</sup> and Fe<sup>3+</sup> ions in oxide materials. *Appl. Surf. Sci.* **2008**, *254* (8), 2441-2449.

- 32. Abdel-Khalek, E.; Motawea, M.; Aboelnasr, M. A.; El-Bahnasawy, H., Study the oxygen vacancies and Fe oxidation states in CaFeO<sub>3-δ</sub> perovskite nanomaterial. *Phys. B: Condens* **2022**, *624*, 413415.
- 33. Zhong, Y.; Yu, L.; Chen, Z.-F.; He, H.; Ye, F.; Cheng, G.; Zhang, Q., Microwave-assisted synthesis of Fe<sub>3</sub>O<sub>4</sub> nanocrystals with predominantly exposed facets and their heterogeneous UVA/Fenton catalytic activity. *ACS Appl. Mater. Interfaces.* **2017**, *9* (34), 29203-29212.
- 34. Hona, R. K.; Ramezanipour, F., Enhanced electrical properties in BaSrFe<sub>2</sub>O<sub>6- $\delta$ </sub> ( $\delta$ = 0.5): A disordered defect-perovskite. *Polyhedron* **2019**, *167*, 69-74.
- 35. Jijil, C. P.; Lokanathan, M.; Chithiravel, S.; Nayak, C.; Bhattacharyya, D.; Jha, S. N.; Babu, P.; Kakade, B.; Devi, R. N., Nitrogen doping in oxygen-deficient Ca<sub>2</sub>Fe<sub>2</sub>O<sub>5</sub>: a strategy for efficient oxygen reduction oxide catalysts. *ACS Appl. Mater. Interfaces.* **2016**, *8* (50), 34387-34395.
- 36. Ghaffari, M.; Liu, T.; Huang, H.; Tan, O.; Shannon, M., Investigation of local structure effect and X-ray absorption characteristics (EXAFS) of Fe (Ti) K-edge on photocatalyst properties of SrTi <sub>(1-x)</sub>FexO<sub>(3-δ)</sub>. *Mater. Chem. Phys.* **2012**, *136* (2-3), 347-357.
- 37. Brown, I.; Altermatt, D., Bond-valence parameters obtained from a systematic analysis of the inorganic crystal structure database. *Acta Crystallographica Section B: Structural Science, Crystal Engineering and Materials* **1985**, *41* (4), 244-247.
- 38. Ramezanipour, F.; Greedan, J. E.; Cranswick, L. M.; Garlea, V. O.; Donaberger, R. L.; Siewenie, J., Systematic Study of Compositional and Synthetic Control of Vacancy and Magnetic Ordering in Oxygen-Deficient Perovskites  $Ca_2Fe_{2-x}Mn_xO_{5+y}$  and  $CaSrFe_{2-x}Mn_xO_{5+y}$  (x=1/2, 2/3, and 1; y=0-1/2). *J. Am. Chem. Soc.* **2012**, *134* (6), 3215-3227.
- 39. Ramezanipour, F.; Cowie, B.; Derakhshan, S.; Greedan, J. E.; Cranswick, L. M., Crystal and magnetic structures of the brownmillerite compound Ca2Fe<sub>1. 039(8)</sub>Mn<sub>0. 962(8)</sub>O<sub>5</sub>. *J. Solid State Chem.* **2009**, *182* (1), 153-159.
- 40. Asenath-Smith, E.; Lokuhewa, I. N.; Misture, S. T.; Edwards, D. D., p-Type thermoelectric properties of the oxygen-deficient perovskite Ca<sub>2</sub>Fe<sub>2</sub>O<sub>5</sub> in the brownmillerite structure. *J. Solid State Chem.* **2010,** *183* (7), 1670-1677.
- 41. Dhankhar, S.; Bhalerao, G.; Baskar, K.; Singh, S. In *Synthesis and characterization of polycrystalline brownmillerite cobalt doped Ca*<sub>2</sub>Fe<sub>2</sub>O<sub>5</sub>, AIP Conference Proceedings, AIP Publishing LLC: 2016; p 140032.
- 42. Li, Q.; Thangadurai, V., A comparative 2 and 4-probe DC and 2-probe AC electrical conductivity of novel co-doped  $Ce_{0.9-x}RExMo_{0.1}O_{2.1-0.5x}$  (RE= Y, Sm, Gd; x= 0.2, 0.3). *J. Mater. Chem.* **2010,** 20 (37), 7970-7983.
- 43. Singh, Y. In *Electrical resistivity measurements: a review*, Int. J. Mod. Phys. Conf. Ser., World Scientific: 2013; pp 745-756.
- 44. Andoulsi, R.; Horchani-Naifer, K.; Ferid, M., Electrical conductivity of La<sub>1-x</sub>Ca<sub>x</sub>FeO<sub>3- $\delta$ </sub> solid solutions. *Ceram. Int.* **2013**, *39* (6), 6527-6531.
- 45. Li, Q.; Sun, L.; Zeng, X.; Zhao, H.; Huo, L.; Grenier, J.-C.; Bassat, J.-M.; Mauvy, F., Evaluation of a brownmillerite oxide as cathode for solid oxide fuel cells. *J. Power Sources* **2013**, *238*, 11-16.
- 46. Inoue, S.; Kawai, M.; Ichikawa, N.; Kageyama, H.; Paulus, W.; Shimakawa, Y., Anisotropic oxygen diffusion at low temperature in perovskite-structure iron oxides. *Nat. Chem* **2010**, *2* (3), 213-217.
- 47. Thangadurai, V.; Beurmann, P. S.; Weppner, W., Mixed oxide ion and electronic conductivity in perovskite-type SrSnO<sub>3</sub> by Fe substitution. *Mater. Sci. Eng.* **2003**, *100* (1), 18-22.
- 48. Shaula, A.; Kharton, V.; Vyshatko, N.; Tsipis, E.; Patrakeev, M.; Marques, F.; Frade, J., Oxygen ionic transport in  $SrFe_{1-y}Al_yO_{3-\delta}$  and  $Sr_{1-x}CaxFe_{0.5}Al_{0.5}O_{3-\delta}$  ceramics. *J. Eur. Ceram. Soc* **2005**, *25* (4), 489-499.
- 49. Cheng, X.; Fabbri, E.; Nachtegaal, M.; Castelli, I. E.; El Kazzi, M.; Haumont, R.; Marzari, N.; Schmidt, T. J., Oxygen evolution reaction on La<sub>1-x</sub> Sr<sub>x</sub>CoO<sub>3</sub> perovskites: a combined experimental and theoretical study of their structural, electronic, and electrochemical properties. *Chem. Mater.* **2015**, *27* (22), 7662-7672.

- 50. Zhang, Q.; Xu, Z.; Wang, L.; Gao, S.; Yuan, S., Structural and electromagnetic properties driven by oxygen vacancy in Sr2FeMoO<sub>6-δ</sub> double perovskite. *J. Alloys Compd.* **2015**, *649*, 1151-1155.
- 51. Vyshatko, N.; Kharton, V.; Shaula, A.; Naumovich, E.; Marques, F., Structural characterization of mixed conducting perovskites La (Ga, M)  $O_{3-\delta}$  (M= Mn, Fe, Co, Ni). *Mater. Res. bull.* **2003**, *38* (2), 185-193.
- 52. Hona, R. K.; Huq, A.; Mulmi, S.; Ramezanipour, F., Transformation of structure, electrical conductivity, and magnetism in AA'Fe<sub>2</sub>O<sub>6- $\delta$ </sub>, A= Sr, Ca and A'= Sr. *Inorg. Chem.* **2017**, *56* (16), 9716-9724.
- 53. Hona, R. K.; Huq, A.; Ramezanipour, F., Unraveling the role of structural order in the transformation of electrical conductivity in  $Ca_2FeCoO_{6-\delta}$ ,  $CaSrFeCoO_{6-\delta}$ , and  $Sr_2FeCoO_{6-\delta}$ . *Inorg. Chem.* **2017,** *56* (23), 14494-14505.
- 54. Sudha, L.; Sukumar, R.; Uma Rao, K., Evaluation of activation energy (Ea) profiles of nanostructured alumina polycarbonate composite insulation materials. *International Journal of Materials*. *Mechanics and Manufacturing* **2014**, *2* (1), 96-100.
- 55. Pizzini, S., *Physical chemistry of semiconductor materials and processes*. John Wiley & Sons: 2015.
- 56. Park, H.; Park, I. J.; Lee, M. G.; Kwon, K. C.; Hong, S.-P.; Kim, D. H.; Lee, S. A.; Lee, T. H.; Kim, C.; Moon, C. W., Water splitting exceeding 17% solar-to-hydrogen conversion efficiency using solution-processed Ni-based electrocatalysts and perovskite/Si tandem solar cell. *ACS Appl. Mater. Interfaces.* **2019**, *11* (37), 33835-33843.
- 57. McCrory, C. C.; Jung, S.; Ferrer, I. M.; Chatman, S. M.; Peters, J. C.; Jaramillo, T. F., Benchmarking hydrogen evolving reaction and oxygen evolving reaction electrocatalysts for solar water splitting devices. *J. Am. Chem. Soc.* **2015**, *137* (13), 4347-4357.
- 58. Zhang, M.; Jeerh, G.; Zou, P.; Lan, R.; Wang, M.; Wang, H.; Tao, S., Recent development of perovskite oxide-based electrocatalysts and their applications in low to intermediate temperature electrochemical devices. *Materials Today* **2021**.
- 59. Li, F.; Han, G.-F.; Noh, H.-J.; Jeon, J.-P.; Ahmad, I.; Chen, S.; Yang, C.; Bu, Y.; Fu, Z.; Lu, Y., Balancing hydrogen adsorption/desorption by orbital modulation for efficient hydrogen evolution catalysis. *Nat. Commun.* **2019**, *10* (1), 1-7.
- 60. Lu, B.; Wahl, C. B.; Lu, X. K.; Sweers, M. E.; Li, H.; Dravid, V. P.; Seitz, L. C., Iridium-Incorporated Strontium Tungsten Oxynitride Perovskite for Efficient Acidic Hydrogen Evolution. *J Solid State Electrochem* **2022**, *144* (30), 13547-13555.
- 61. Muratore, G.; Rizzo, V.; Licciardello, F.; Maccarone, E., Partial dehydration of cherry tomato at different temperature, and nutritional quality of the products. *Food Chem.* **2008**, *111* (4), 887-891.
- 62. Zhang, W.; Li, H.; Firby, C. J.; Al-Hussein, M.; Elezzabi, A. Y., Oxygen-vacancy-tunable electrochemical properties of electrodeposited molybdenum oxide films. *ACS Appl. Mater. Interfaces.* **2019**, *11* (22), 20378-20385.
- 63. Kananke-Gamage, C. C.; Ramezanipour, F., Structure Effect on Pseudocapacitive Properties of A2LaMn2O7 (A= Ca, Sr). *Energy Technology*.
- 64. Kananke-Gamage, C. C.; Ramezanipour, F., Variation of the electrocatalytic activity of isostructural oxides Sr<sub>2</sub>LaFeMnO<sub>7</sub> and Sr<sub>2</sub>LaCoMnO<sub>7</sub> for hydrogen and oxygen-evolution reactions. *Dalton Trans.* **2021**, *50* (40), 14196-14206.
- 65. Li, Y. H.; Liu, P. F.; Pan, L. F.; Wang, H. F.; Yang, Z. Z.; Zheng, L. R.; Hu, P.; Zhao, H. J.; Gu, L.; Yang, H. G., Local atomic structure modulations activate metal oxide as electrocatalyst for hydrogen evolution in acidic water. *Nat. Commun.* **2015**, *6* (1), 8064.
- 66. Murthy, A. P.; Theerthagiri, J.; Madhavan, J., Insights on Tafel constant in the analysis of hydrogen evolution reaction. *J. Phys. Chem. C* **2018**, *122* (42), 23943-23949.
- 67. Peng, Z.; Wang, K.; Xu, W.; Wang, B.; Mao, B.; Han, Y.; Tsung, C.-K.; Yang, B.; Liu, Z.; Li, Y., Strong interface enhanced hydrogen evolution over molybdenum-based catalysts. *ACS Appl. Energy Mater.* **2020**, *3* (6), 5219-5228.

- 68. Ling, C.; Ouyang, Y.; Shi, L.; Yuan, S.; Chen, Q.; Wang, J., Template-grown MoS<sub>2</sub> nanowires catalyze the hydrogen evolution reaction: ultralow kinetic barriers with high active site density. *ACS Catal.* **2017**, *7* (8), 5097-5102.
- 69. Shinagawa, T.; Garcia-Esparza, A. T.; Takanabe, K., Insight on Tafel slopes from a microkinetic analysis of aqueous electrocatalysis for energy conversion. *Sci. Rep.* **2015**, *5* (1), 1-21.
- 70. Konkena, B.; Sinev, I.; Piontek, S.; Khavryuchenko, O.; Dürholt, J. P.; Schmid, R.; Tüysüz, H.; Muhler, M.; Schuhmann, W.; Apfel, U.-P., Pentlandite rocks as sustainable and stable efficient electrocatalysts for hydrogen generation. *Nat. Commun.* **2016**, *7* (1), 1-8.
- 71. Pan, Y.; Chen, Y.; Li, X.; Liu, Y.; Liu, C., Nanostructured nickel sulfides: phase evolution, characterization and electrocatalytic properties for the hydrogen evolution reaction. *RSC Adv.* **2015**, *5* (127), 104740-104749.
- 72. Alom, M. S.; Ramezanipour, F., Vacancy effect on the electrocatalytic activity of LaMn<sub>1/2</sub>Co<sub>1/2</sub>O<sub>3- $\delta$ </sub> for hydrogen and oxygen evolution reactions. *Chem. Commun.* **2023**, *59*, 5870-5873.
- 73. Suntivich, J.; Hong, W. T.; Lee, Y.-L.; Rondinelli, J. M.; Yang, W.; Goodenough, J. B.; Dabrowski, B.; Freeland, J. W.; Shao-Horn, Y., Estimating hybridization of transition metal and oxygen states in perovskites from Ok-edge x-ray absorption spectroscopy. *J. Phys. Chem. C* **2014**, *118* (4), 1856-1863.
- 74. Bocquet, A.; Mizokawa, T.; Saitoh, T.; Namatame, H.; Fujimori, A., Electronic structure of 3d-transition-metal compounds by analysis of the 2p core-level photoemission spectra. *Phys. Rev. B* **1992**, *46* (7), 3771.
- 75. Torrance, J.; Lacorre, P.; Nazzal, A.; Ansaldo, E.; Niedermayer, C., Systematic study of insulator-metal transitions in perovskites RNiO<sub>3</sub> (R= Pr, Nd, Sm, Eu) due to closing of charge-transfer gap. *Phys. Rev. B* **1992**, *45* (14), 8209.

# **Table of Contents**

The electrocatalytic activity for hydrogen evolution reaction (HER) and its correlation with structural order, transition metal type, and electrical conductivity is demonstrated for  $Ca_3Fe_{3-x}Mn_xO_8$  (x = 1 - 2). The increase in structural order is associated with an increase in electrical conductivity and enhancement of the electrocatalytic activity for HER in acidic conditions.

